RSC Advances

PAPER

View Article Online
View Journal | View Issue

Cite this: *RSC Adv.*, 2025, **15**, 13583

Self-sacrificial synthesis of $Cu_3(HHTP)_2$ on Cu substrate for recyclable NH_3 gas adsorption with energy-efficient photothermal regeneration†

Soyeon Jin,[a] Jinwook Lee,[a] Sunjeong Kim,[a] Gyeong Chan Kim,[b] Jung-Hoon Yun[bc] and Jooyoun Kim *[ad]

The efficient adsorption and removal of toxic gases, particularly ammonia (NH_3), remains a critical challenge in environmental management and industrial safety. Metal–organic frameworks (MOFs) have emerged as promising gas adsorbents due to their tunable structures and high surface area. However, the strong interaction between NH_3 and MOFs poses challenges for the regeneration and reusability of MOF adsorbents, often requiring energy-intensive desorption methods. This study proposes a sustainable approach for regenerating adsorption sites for recyclable gas adsorbents. We present a facile method for the direct synthesis of $Cu_3(HHTP)_2$ on a Cu mesh substrate ($Cu_3(HHTP)_2$@Cu), utilizing the Cu metal itself as a precursor to eliminate the need for external metal sources. The resulting $Cu_3(HHTP)_2$@Cu serves as a recyclable NH_3 adsorbent, leveraging the π-conjugated hexahydroxytriphenylene (HHTP) ligand for photothermal conversion under sunlight irradiation, where photo-generated heat facilitates NH_3 desorption. The study further explores the effect of an external voltage on the NH_3 adsorption performance and crystalline structure of $Cu_3(HHTP)_2$@Cu. Our findings demonstrate that $Cu_3(HHTP)_2$@Cu achieves efficient NH_3 desorption through a minimally invasive and energy-efficient mechanism, addressing the limitations of conventional adsorbents.

Received 26th February 2025
Accepted 22nd April 2025

DOI: 10.1039/d5ra01388g

rsc.li/rsc-advances

1. Introduction

The efficient adsorption and removal of toxic gases remains a critical challenge in environmental management and industrial safety.[1–3] Among various gas adsorption strategies, porous crystalline materials such as zeolites, activated carbon, metal–organic frameworks (MOFs), and hybrid porous materials have emerged as promising gas adsorbents due to their high surface area.[4–7] Particularly, MOFs, composed of metal nodes coordinated with organic ligands, are advantageous as effective adsorbents with their tunable chemical compositions and abundant active sites.[8–10] Among various toxic gases, ammonia (NH_3) is of particular concern due to its high toxicity and corrosive nature.[11,12] As a polar molecule, NH_3 interacts with MOFs through multiple interactions including hydrogen bonding, coordination bonding (acting as a Lewis base), and van der Waals interaction, allowing its selective adsorption by MOF-based adsorbents.[13,14]

Optimizing the adsorption performance of MOFs can be achieved through structural and chemical modifications, framework deformation, or enhancing pore accessibility *via* external stimuli like an electric field.[15–17] These treatments may improve interactions between MOFs and target adsorbates, leading to enhanced adsorption capacity and selectivity. However, when the interactions between NH_3 and the adsorption sites are too strong, it requires higher energy to detach the adsorbed molecules, posing restraints in regenerating adsorption sites for the reusability of adsorbents.[18,19] To address this challenge, various regeneration strategies have been explored including thermally activated and decompression-based desorption.[16] However, thermal treatment demands significant energy input, and the adsorbent requires structural robustness to maintain structural integrity throughout repeated thermal-desorption cycles. Also, decompression-based regeneration alone is insufficient for the complete detachment of strongly adsorbed molecules, thus it is typically combined with thermal treatments to facilitate desorption.[20,21]

While those regeneration methods often require energy input, photothermal desorption has drawn attention as an energy-efficient and non-invasive approach to gas desorption.[22,23] Unlike thermal treatments, photothermal conversion harnesses sunlight to generate heat without additional energy

[a]*Department of Fashion and Textiles, Seoul National University, Seoul, 08826, Republic of Korea. E-mail: jkim256@snu.ac.kr*
[b]*Department of Future Convergence Engineering, Kongju National University, Cheonan, 31080, Republic of Korea*
[c]*Department of Mechanical and Automotive Engineering, Kongju National University, Cheonan, 31080, Republic of Korea*
[d]*Research Institute of Human Ecology, Seoul National University, Seoul, 08826, Republic of Korea*

† Electronic supplementary information (ESI) available. See DOI: https://doi.org/10.1039/d5ra01388g

input or mechanical stress.[24,25] By utilizing solar energy, adsorption sites can be regenerated for repeated gas adsorption while minimizing structural alterations of adsorbents and ensuring long-term stability.[26,27] Effective photothermal materials should exhibit broad solar absorption and convert the absorbed light energy into heat primarily *via* non-radiative decay pathways, rather than losing energy through fluorescence in the form of radiative relaxation.[28,29] For the MOFs that have restricted light absorption efficiency, the excited electrons commonly return to the ground state predominantly through radiative relaxation, resulting in the emission of photon rather than heat.[30,31]

To overcome this limitation, MOFs have been hybridized with other photothermal-active materials such as carbon-based nanostructures or plasmonic nanoparticles, thereby improving light-harvesting capability and thermal energy conversion efficiency.[32,33] For instance, Pornea *et al.*[34] developed a hybrid MOF shell composed of PCN-224 and Prussian blue and attained photothermal conversion with broad solar absorption, demonstrating the temperature increase from 33 °C to 56 °C. Zhu *et al.*[35] applied a 3D stacked MOF nanosheet (CASFZU-1) incorporated with Pd particles for improved photothermal conversion, increasing temperature from about 40 °C to 54 °C. Recent developments demonstrated the application of photothermal performance for low-energy gas desorption. Liu *et al.*[23] applied the photothermal ability to develop a recyclable adsorbent against ethyl acetate vapor, integrating graphene oxide nanosheets with MIL-101, where the resulting material showed stable adsorption–desorption performance during five cycles of use. Zhou *et al.*[20] integrated reduced graphene oxide with MOF-303 and achieved photothermally induced desorption up to 67.6%. While those studies demonstrated the potential application of photothermal ability to gas desorption by combining graphene-type material with porous MOFs, challenges remain in exploring the facile and simple process for synthesizing photothermally recyclable adsorbent. Herein, recent efforts have turned to conductive MOFs, which inherently possess light-to-heat conversion capability and thus eliminate the need for external photothermal agents.[36–38] Unlike most MOFs that are electrically insulating, conductive MOFs feature highly conjugated organic linkers coordinated with metal nodes, forming a narrow band gap between the valence and conduction band that enhances light absorption.[39–44] As photoexcited electrons in conductive MOFs relax back to the lower-energy state, they predominantly undergo non-radiative relaxation, efficiently converting absorbed energy into heat and transferring it to surrounding molecules *via* vibrations and collisions.[45–47]

Speculating that $Cu_3(HHTP)_2$ would allow for effective gas adsorption and photothermally-induced regeneration of adsorption sites, this study explores experimental investigations to develop a recyclable gas adsorbent. A facile approach for synthesizing $Cu_3(HHTP)_2$ onto Cu mesh was explored, using the Cu mesh as a self-sacrificial substrate for sourcing metal precursor, in forming $Cu_3(HHTP)_2$. By adding only the HHTP ligand, $Cu_3(HHTP)_2$ was grown directly on the Cu mesh ($Cu_3(HHTP)_2$@Cu). The primary goal is to develop $Cu_3(HHTP)_2$@Cu as a recyclable NH_3 gas adsorbent, leveraging π-conjugated HHTP ligand for photothermal conversion of sunlight. In this system, generated heat facilitates the desorption of adsorbed gas molecules, leading to efficient regeneration of adsorption sites.

Additionally, the effect of external voltage applied to $Cu_3(HHTP)_2$@Cu on NH_3 adsorption and desorption performance is examined, focusing on its influence on the structural deformation of $Cu_3(HHTP)_2$ MOF. The photothermal conversion capability of $Cu_3(HHTP)_2$ is analyzed in association with NH_3 desorption performance and the recyclability of $Cu_3(HHTP)_2$@Cu as an adsorbent. The key feature of this work lies in the integrated design of $Cu_3(HHTP)_2$ MOF with a metal substrate for multiple effects as: (1) sustainable synthesis of $Cu_3(HHTP)_2$ using Cu substrate as a metal precursor source without external addition of metallic compound, (2) facilitated photothermal effect *via* Cu metal's thermal conductivity, and (3) electrical conductivity leveraged for potential improvement in gas adsorption with voltage application. This work addresses the limited recyclability of conventional gas adsorbents and demonstrates a minimally invasive and sustainable desorption mechanism. The findings are anticipated to offer an informative discussion for developing an effective recyclable gas adsorbent with energy-efficient regeneration strategies.

2. Experimental methods

2.1 Synthesis of $Cu(OH)_2$ on Cu mesh ($Cu(OH)_2$@Cu)

A Cu mesh (3 cm × 3 cm) was sonicated with ethanol and distilled water for 15 min to ensure a clean surface, respectively. The cleaned Cu mesh was then immersed in a 80 mL of mixed aqueous solution of 4 M NaOH and 0.2 M $(NH_4)_2S_2O_8$ with a volume ratio of 1 : 1 at room temperature (25 ± 3 °C) for 20 min. Subsequently, it was washed with distilled water three times and dried at room temperature overnight, yielding the Cu mesh with grown $Cu(OH)_2$ nanostructures ($Cu(OH)_2$@Cu).

2.2 Synthesis of $Cu_3(HHTP)_2$ on Cu mesh ($Cu_3(HHTP)_2$@Cu)

1.8 mM of hexahydroxytriphenylene (HHTP) aqueous solution was prepared by dissolving 0.1 mmol of HHTP in 55 mL of distilled water and DMF with a volume ratio of 10 : 1. When they were completely dissolved, the $Cu(OH)_2$@Cu mesh was immersed into the solution and placed in an oven at 70 °C for 1 h. Following the reaction, the resulting $Cu_3(HHTP)_2$ MOF grown at Cu mesh (denoted as $Cu_3(HHTP)_2$@Cu) was cooled to room temperature and washed with distilled water. After that, the $Cu_3(HHTP)_2$@Cu was dried overnight at 40 °C.

2.3 Gas adsorption and desorption evaluation

The adsorption performance of $Cu_3(HHTP)_2$@Cu against ammonia (NH_3) gas was measured in a static condition in a Tedlar bag. Before gas adsorption test, $Cu_3(HHTP)_2$@Cu (1.5 cm × 1.5 cm) was kept at 70 °C for 1 h to remove any residual solvent in MOF pores. The pretreated $Cu_3(HHTP)_2$@Cu was placed in a 10 L Tedlar bag (Supelco, PA) filled with 5 L of 23 ppm of NH_3 gas where N_2 (99.99%) was used as a diluent gas.

The NH_3 concentration was monitored by the detector (Gastiger 6000, Wandi, China) at 25 °C. The experimental setup is presented in Fig. S1.† The ambient NH_3 concentration was measured after reaching adsorption equilibrium, and the adsorption was calculated using eqn (1).

$$\text{Adsorption}\left(\text{mmol g}^{-1}\right) = \frac{\text{Injected NH}_3\text{(mmol)} - \text{residual NH}_3\text{(mmol)}}{\text{Weight of Cu}_3\text{(HHTP)}_2\text{(g)}} \quad (1)$$

To test the gas adsorption performance with external voltage applied to $Cu_3(HHTP)_2$@Cu, a DC power of 1 V (UTP3315TFL-II, UNI-Trend Technology Co., Ltd, China) was applied. Electrodes connected to the DC power supply were inserted into the Tedlar bag with $Cu_3(HHTP)_2$@Cu, and the current was monitored by a digital multimeter (Keithley DMM 6500, Keithley Instruments, LLC, USA). Intending to use $Cu_3(HHTP)_2$@Cu as a recyclable gas adsorbent, the desorption performance of $Cu_3(HHTP)_2$@Cu was examined. To evaluate the photothermal conversion effect, temperature changes of the $Cu_3(HHTP)_2$@Cu surface (3 cm × 3 cm) were recorded at 1 min intervals over a total period of 10 min, including 5 min of light irradiation and a subsequent 5 min period without irradiation, using an infrared camera (FLIR C5 1.2, Teledyne FLIR LLC, USA). To investigate the photothermal conversion performance, the temperature changes of $Cu_3(HHTP)_2$@Cu was compared with those of $Cu(OH)_2$@Cu and $Cu_3(HHTP)_2$ crystals. A xenon lamp (150 W) was used to provide one-sun illumination with a power density of 100 mW cm^{-2}.

The NH_3 desorption amount of $Cu_3(HHTP)_2$@Cu mesh was measured after NH_3 adsorption by the same Tedlar bag setup with 5 L of 23 ppm NH_3. Allowing adsorption to proceed over 20 h to ensure sufficient time for equilibrium, the residual gas in the Tedlar bag was completely removed, and 5 L of N_2 (99.9%) of fresh gas was injected into a Tedlar bag. The gas detector monitored the concentration of NH_3 desorbed from $Cu_3(HHTP)_2$@Cu in the Tedlar bag (Gastiger 6000, Wandi, China). As shown in Table 1, $Cu_3(HHTP)_2$@Cu was subjected to different adsorption and desorption treatments. The desorption amount for $Cu_3(HHTP)_2$@Cu was compared for two different treatments, light irradiation and heating. For the heating condition, a $Cu_3(HHTP)_2$@Cu-containing Tedlar bag was placed in direct contact with a heating plate while shielding it from light. This setup ensured that the $Cu_3(HHTP)_2$@Cu material reached a temperature of 55 °C, matching the temperature induced by light exposure. As a control, the Tedlar bag was maintained at room temperature (25 ± 3 °C) and covered with a dark box to block any light. To evaluate the reusability of $Cu_3(HHTP)_2$@Cu, the NH_3 adsorption–desorption cyclic test was conducted following the same procedures described above. The $Cu_3(HHTP)_2$@Cu sample underwent 20 h of adsorption followed by 2 h of desorption, and this cycle was repeated up to seven times.

2.4 DFT simulation

The simulations were conducted using Gaussian 16 with a semi-empirical approach based on the PM6 Hamiltonian.[48] For a focused analysis of the adsorption process, a slab model of the Cu-HHTP framework was selected as the target for the simulation of NH_3 adsorption on $Cu_3(HHTP)_2$. The adsorption energy of NH_3 was calculated by evaluating the enthalpy change before and after NH_3 adsorption at specific symmetric reduced sites.

3. Results and discussion

3.1 Structural characterization of $Cu_3(HHTP)_2$@Cu

Utilizing Cu mesh as a substrate and source of Cu metal precursor, $Cu_3(HHTP)_2$ was directly synthesized on the Cu mesh *via* a self-sacrificial process without external addition of metal precursor. In this process, the Cu mesh plate underwent chemical oxidation, forming blue-colored $Cu(OH)_2$ nanowires in about 4 μm length and 200–400 nm width (Fig. 1c, d and S2b†). The $Cu_3(HHTP)_2$ was grown on top of $Cu(OH)_2$ nanowires by adding only HHTP ligands. As a result, hexagonal rod-like $Cu_3(HHTP)_2$ crystals in 1–2 μm length grew radially along the $Cu(OH)_2$ nanowires, turning black (Fig. 1e, f and S2c†). The elemental mapping of Cu, C, and O in Fig. 1a, c, and 1d indicate the uniform distribution of $Cu_3(HHTP)_2$@Cu on the surface As shown in Fig. 1b, the X-ray diffraction (XRD) patterns of $Cu_3(HHTP)_2$@Cu exhibit well-defined crystalline peaks that align with the simulated pattern of $Cu_3(HHTP)_2$ crystal, with characteristic peaks at $2\theta = 4.86°$, 9.76°, 12.68°, and 28.24°, corresponding to the [100], [200], [210], and [002] planes.

The loaded weight % $Cu_3(HHTP)_2$ was determined using thermogravimetric analysis (TGA) (Fig. 2). Upon heating to 600 °C, the $Cu(OH)_2$@Cu exhibited minimal weight loss (<0.3%), confirming its thermal stability. $Cu_3(HHTP)_2$ crystal showed a weight loss of 74.7% when the temperature reached 600 °C. Based on the weight loss of the $Cu_3(HHTP)_2$@Cu, the $Cu_3(HHTP)_2$ loading on the Cu substrate was calculated to be 3.3% by eqn (2), where X is the weight fraction of $Cu_3(HHTP)_2$, and $WL_{MOF+Mesh}$, WL_{MOF}, and WL_{Mesh} are the weight loss of $Cu_3(HHTP)_2$@Cu, $Cu_3(HHTP)_2$ crystal, and $Cu(OH)_2$@Cu,

Table 1 Different adsorption–desorption treatments of $Cu_3(HHTP)_2$@Cu sample

Sample	Adsorption treatment	Desorption treatment
$Cu_3(HHTP)_2$@Cu-C	No voltage	Room temperature (control)
$Cu_3(HHTP)_2$@Cu-T1	No voltage	Thermal treatment (55 °C)
$Cu_3(HHTP)_2$@Cu-T2	No voltage	Photothermal conversion (one sun irradiation)
$Cu_3(HHTP)_2$@Cu-T3	Applied 1 V	Photothermal conversion (one sun irradiation)

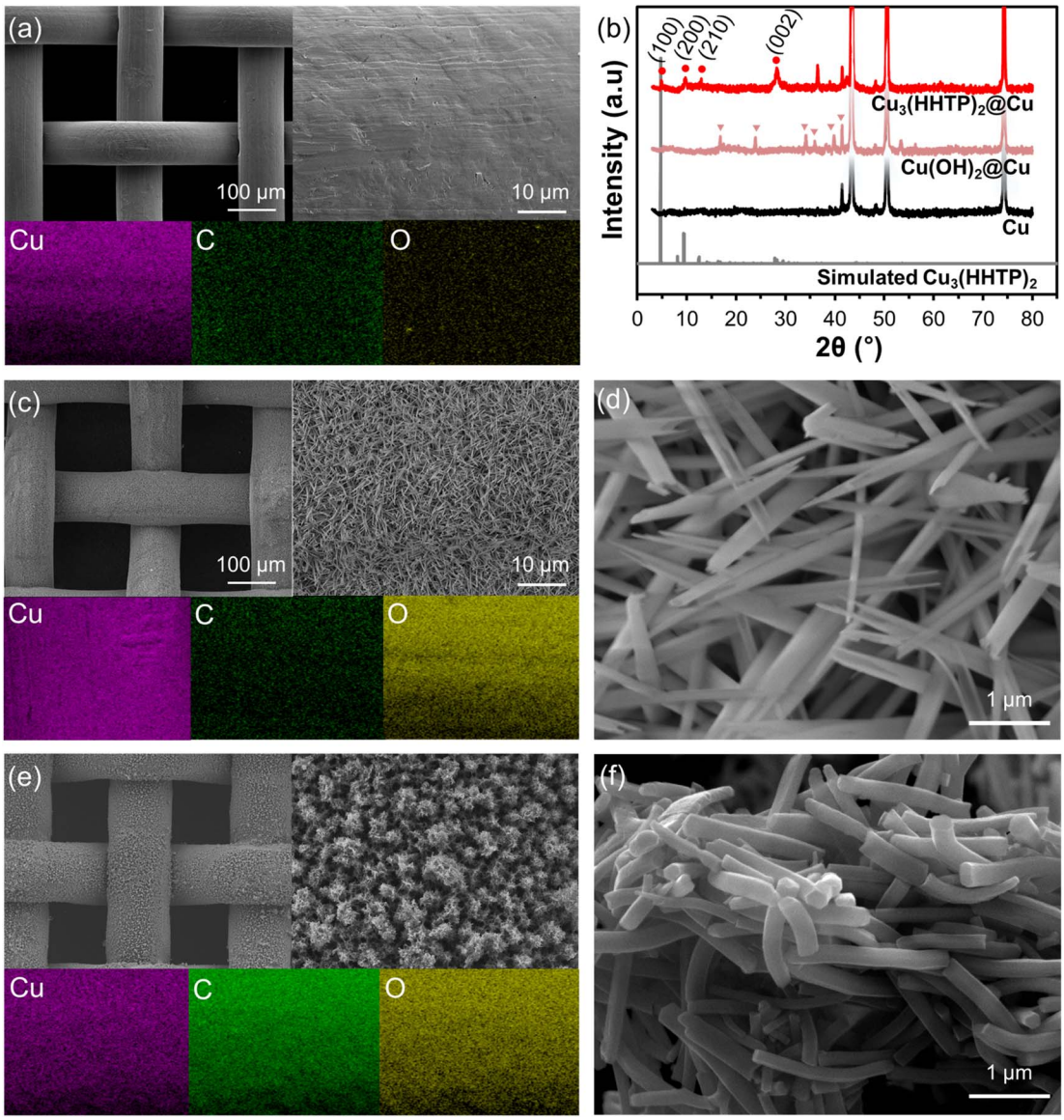

Fig. 1 Scanning electron microscopy (SEM) images and elemental mapping of (a) Cu mesh, (c and d) $Cu(OH)_2$@Cu, (e and f) $Cu_3(HHTP)_2$@Cu, and (b) X-ray diffraction (XRD) patterns.

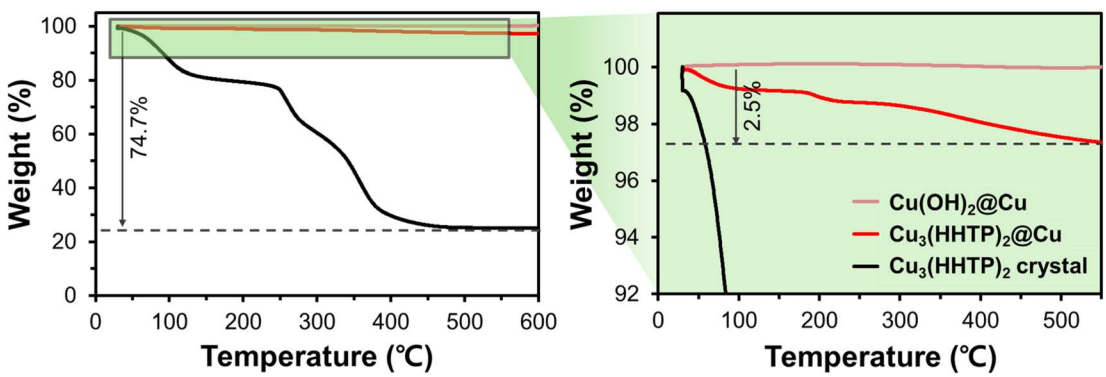

Fig. 2 Thermogravimetric analysis (TGA) curve of $Cu_3(HHTP)_2$.

respectively. The TGA and XRD analyses confirmed the successful synthesis of $Cu_3(HHTP)_2$ on the Cu substrate.

$$WL_{MOF+Mesh} = WL_{MOF} \cdot X + WL_{Mesh} \cdot (1 - X) \quad (2)$$

3.2 NH_3 gas adsorption by $Cu_3(HHTP)_2$@Cu

The NH_3 adsorption performance of $Cu_3(HHTP)_2$@Cu was evaluated under dark conditions. The time-dependent adsorption performance of $Cu_3(HHTP)_2$@Cu was presented in Fig. 3a, where the NH_3 concentration gradually decreased, reaching an adsorption performance of 83.5% in 120 min. In comparison, $Cu_3(HHTP)_2$@Cu under 1 V achieved nearly complete NH_3 removal, with 99.9% adsorption within 2 h. The NH_3 adsorption kinetics were analyzed based on a pseudo-first-order kinetics model, and the corresponding rate constant (k) and half-time ($t_{1/2}$) values, calculated using $t_{1/2} = 0.693/k$, are presented in Fig. S3.† A significant enhancement in NH_3 adsorption kinetics was observed upon applying voltage, as the half-time ($t_{1/2}$) decreased from approximately 23 min (without voltage) to 12 min (with 1 V). As prior studies reported that the application of an electric field enhanced gas adsorption, the effect of applied voltage on gas adsorption was investigated in Fig. 3b, comparing the NH_3 adsorption performance of $Cu_3(HHTP)_2$@Cu under 0 V and 1 V, respectively. Given that $Cu_3(HHTP)_2$@Cu adsorbs nearly all introduced NH_3 under 23 ppm after extended adsorption time of over 20 h, the adsorption capacity test was performed at a higher NH_3 concentration of 46 ppm to better compare the effect of applied voltage. After 20 h of NH_3 exposure (under 0 V), $Cu_3(HHTP)_2$@Cu adsorbed 1.6 mmol of NH_3 per gram of loaded $Cu_3(HHTP)_2$. Under an applied voltage of 1 V, $Cu_3(HHTP)_2$@Cu adsorbed 2.1 mmol of NH_3 per gram of loaded $Cu_3(HHTP)_2$, representing a 31% increase compared to the condition without voltage application.

To analyze the effects of electric voltage on the surface chemistry and bonding interactions of $Cu_3(HHTP)_2$, X-ray photoelectron spectroscopy (XPS) was carried out. As shown in Fig. 4a and b, regardless of the applied electric voltage, $Cu_3(HHTP)_2$ exhibited peaks at 954.0 eV (Cu $2p_{1/2}$) and 934.1 eV (Cu $2p_{3/2}$). The Cu $2p_{1/2}$ peak was deconvoluted into three components, Cu^{2+} (956.3 eV), Cu^+ (954.2 eV), and Cu^0 (952.3 eV), and the Cu $2p_{3/2}$ peak was deconvoluted into Cu^{2+} (936.8 eV), Cu^+ (934.4 eV), and Cu^0 (932.6 eV).[49] The presence of Cu^+ and Cu^0 suggests the partial reduction of Cu^{2+} during Cu–O formation in $Cu_3(HHTP)_2$. Notably, the Cu species, which can act as coordinatively unsaturated sites, serve as Lewis acid within the structure, facilitating interactions with the lone pairs of NH_3. This suggests that the NH_3 adsorption performance of $Cu_3(HHTP)_2$ is enhanced by the unsaturated Cu sites available in $Cu_3(HHTP)_2$. In Fig. 4b, the ratio of $Cu^{2+}/[Cu^+ + Cu^0]$ increased from 0.2 to 0.3, and this increased Cu^{2+} ratio implies that Cu–O bonds were weakened, modifying the coordination environment of $Cu_3(HHTP)_2$ under electric voltage. Similar results are observed in the O 1s region, where four prominent peaks attributed to –OH (533.6 eV), C–O (532.7 eV), C═O (531.6 eV), and Cu–O (530.5 eV) are shown.[50] Applying 1 V, the area of Cu–O decreased, demonstrating the weakened coordination interactions between Cu metal center and HHTP ligands.

To examine the effect of electric voltage on the porous characteristics, BET analysis was performed on $Cu_3(HHTP)_2$@Cu before and after applying 1 V electric voltage, as shown in Fig. 5. Notably, the surface area increased from 79.0 $m^2\ g^{-1}$ to 158.7 $m^2\ g^{-1}$ after voltage application to $Cu_3(HHTP)_2$@Cu, reaching nearly twice its initial surface area; this increased surface area provides more adsorption sites and opportunities for interaction with NH_3. Based on XPS and BET analyses, it can be concluded that the enhanced NH_3 adsorption performance of $Cu_3(HHTP)_2$@Cu under 1 V is attributed to the deformation of coordination bonding between the Cu metal centers and HHTP ligands within the MOF. Electrical stimulation causes structural modifications, increasing the accessible surface area and the active adsorption sites, which leads to significant enhancement in NH_3 adsorption.

3.3 DFT simulation of NH_3 adsorption on $Cu_3(HHTP)_2$@Cu

To provide molecular-level insights into the NH_3 adsorption mechanism, density functional theory (DFT) simulation was carried out for $Cu_3(HHTP)_2$@Cu, with and without voltage application. Since applying voltage does not always lead to the formation of a regular current flow within the MOF, the NH_3 adsorption simulation was carried out by assuming the

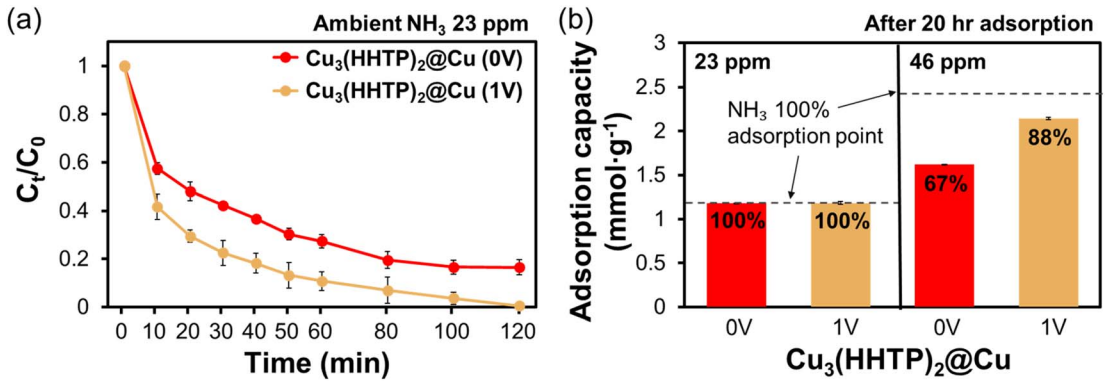

Fig. 3 NH_3 adsorption with and without voltage. (a) NH_3 adsorption for 2 h at 23 ppm NH_3, (b) NH_3 adsorption efficiency (%) and capacity per g of $Cu_3(HHTP)_2$ crystals attached on Cu mesh under 23 ppm and 46 ppm NH_3.

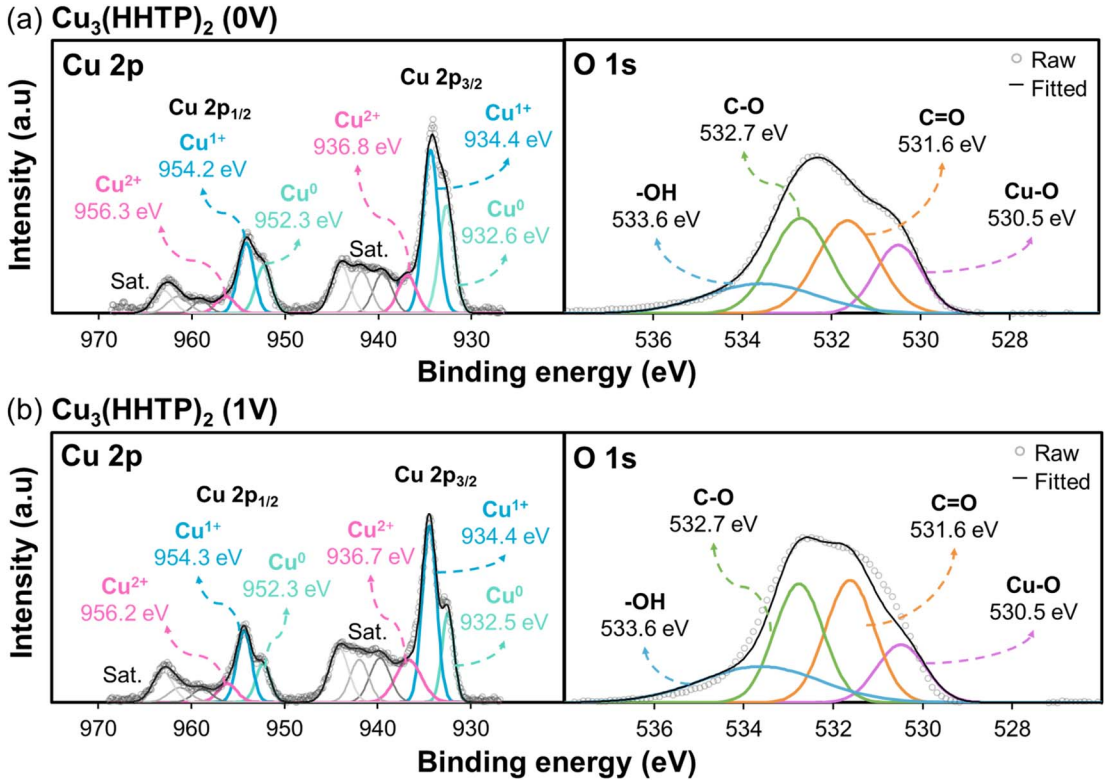

Fig. 4 High-resolution Cu 2p and O 1s XPS spectra for (a) $Cu_3(HHTP)_2$ without external electric voltage and (b) $Cu_3(HHTP)_2$ after 1 V applied.

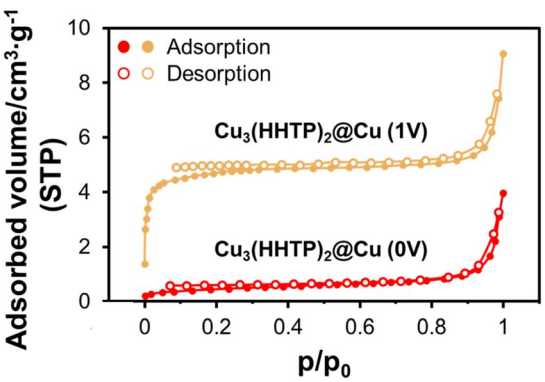

Fig. 5 N_2 adsorption–desorption isotherms of $Cu_3(HHTP)_2$@Cu with and without external electric voltage.

addition of electrons to represent the 1 V condition. The potential NH_3 adsorption sites on $Cu_3(HHTP)_2$ were shown in Fig. 6a–c, and corresponding adsorption energies were calculated, as shown in Table 2. From the DFT results, electron-charged $Cu_3(HHTP)_2$ exhibited lower (more negative) adsorption energies compared to uncharged $Cu_3(HHTP)_2$, suggesting stronger binding interactions were constructed between NH_3 and $Cu_3(HHTP)_2$. Particularly, the Cu neighbor site (−0.121 eV) and the hydrogen-rich site (−0.114 eV) exhibit the lowest adsorption energies for charged $Cu_3(HHTP)_2$, indicating that these two sites are the most favorable for NH_3 adsorption. A comparative analysis of adsorption sites reveals distinct adsorption mechanisms. At the Cu neighbor site, adsorption is primarily governed by charge affinity between the O and H atoms, which facilitates electron delocalization between the NH_3 molecule and the Cu metal center (Fig. 6b). In contrast, at the hydrogen-rich site, electrostatic interactions between the N and H atom of NH_3 were dominant, as shown in Fig. 6c. Overall, the DFT results indicate that the electron charge on $Cu_3(HHTP)_2$ enhances NH_3 adsorption by promoting the charge delocalization at Cu neighbor sites. This increases the interaction between the NH_3 molecule and the Cu center, suggesting the possibility of a charge-mediated adsorption mechanism. These results are further corroborated by experimental results, which indicate improved adsorption under a 1 V external electric voltage.

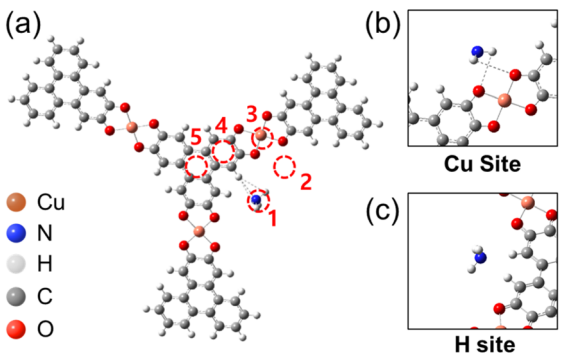

Fig. 6 Simulation of NH_3 adsorption. (a) Various adsorption sites, (b) Cu site, and (c) H site.

Table 2 Adsorption energy (eV) of NH_3 molecule on various adsorption sites of $Cu_3(HHTP)_2$

Site no.	Charge	Electron E (eV)
1	2	−0.114
2	2	−0.121
3	2	−0.111
4	2	0.0144
5	2	0.0144
1	0	1.16
2	0	2.24
3	0	0.662
4	0	1.14
5	0	1.03

3.4 Photothermal conversion effect

The $Cu_3(HHTP)_2$@Cu was intended for application as a recyclable gas adsorbent, leveraging the photothermal conversion effect of $Cu_3(HHTP)_2$ for the minimally invasive gas desorption method. Photothermal conversion occurs when photo-excited electrons by light absorption undergo transitions of molecular orbitals within the conduction band, leading to non-radiative relaxation and heat generation. Conductive MOFs like $Cu_3(HHTP)_2$ develop well-defined π–π* interactions between HHTP ligands, resulting in a narrow band gap and a wider range of wavelengths for efficient light absorbance. In Fig. S4,† compared to bare Cu and $Cu(OH)_2$@Cu, the light absorbance of $Cu_3(HHTP)_2$@Cu shows enhancement across the entire UV-visible region, attributed to the π-conjugation in the HHTP ligand. With the small energy gap between the excited and ground states attributed to the π-conjugation, thermal vibration, rather than fluorescence or photon emission, can efficiently relax the molecule. Thus, HHTP often shows efficient photothermal conversion with non-radiative relaxation.

Fig. 7 shows the photothermal conversion performance of Cu, $Cu(OH)_2$@Cu, $Cu_3(HHTP)_2$ crystal sheet, and $Cu_3(HHTP)_2$@Cu demonstrated by surface temperatures with and without light exposure. Under one-sun irradiation, the temperature of $Cu_3(HHTP)_2$@Cu rose rapidly within 1 min and

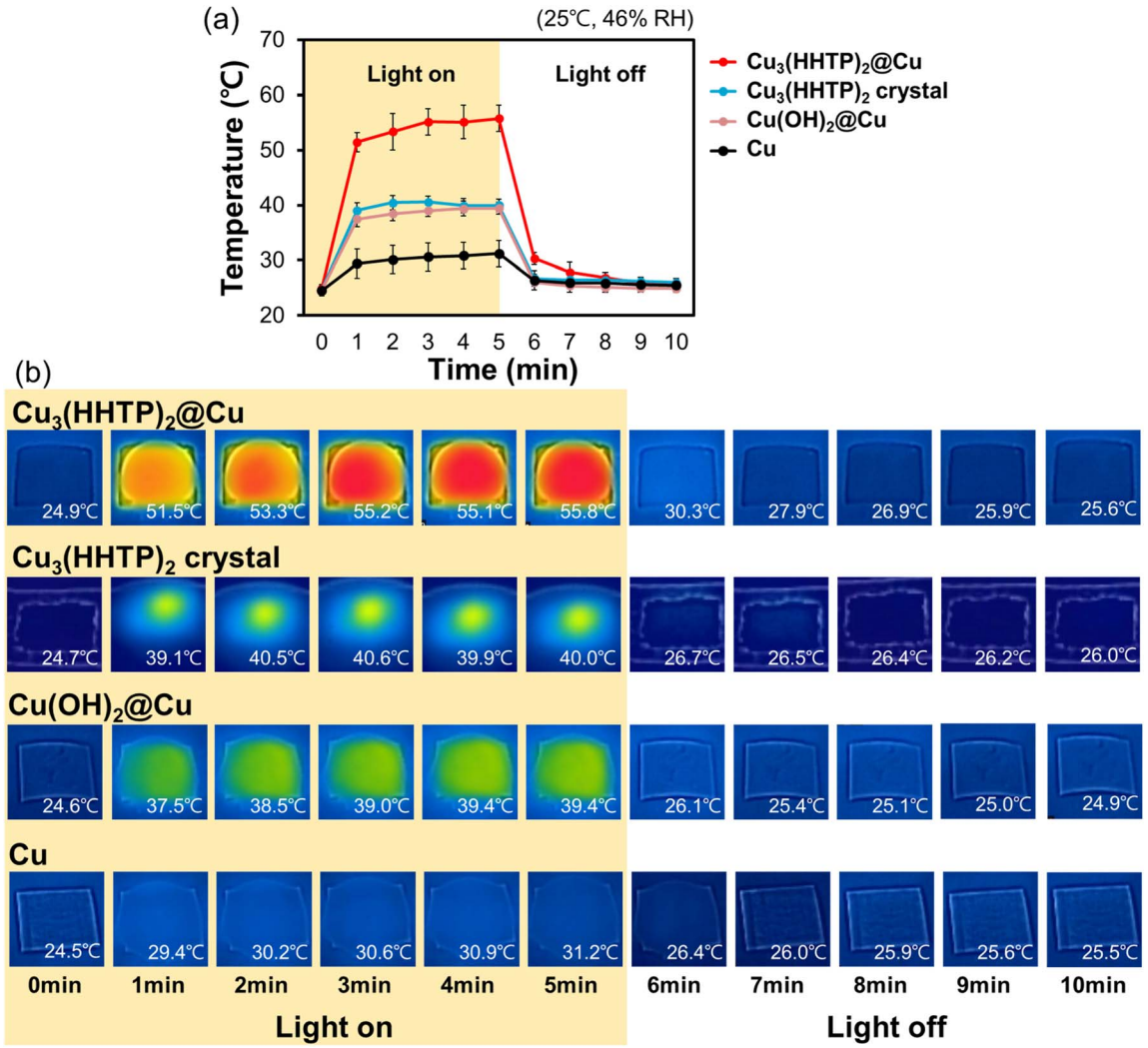

Fig. 7 Photothermal conversion effects demonstrated by (a) surface temperature changes and (b) infrared images for Cu, $Cu(OH)_2$@Cu, $Cu_3(HHTP)_2$ crystal, and $Cu_3(HHTP)_2$@Cu.

it dropped immediately after turning off the light, indicating that the temperature change was solely driven by the light-induced reaction. After 5 min of irradiation, the surface temperature of each sample increased from the base temperature of 25 °C as follows: Cu mesh, 31.2 °C (~27% increase); $Cu(OH)_2$@Cu, 39.4 °C (~61% increase); $Cu_3(HHTP)_2$ crystal sheet, 40.7 °C (~63% increase); $Cu_3(HHTP)_2$@Cu, 55.8 °C (~124% increase). $Cu(OH)_2$@Cu exhibited slightly enhanced photothermal conversion compared to Cu mesh because $Cu(OH)_2$@Cu can absorb a broader range of light (Fig. S3†), resulting in a higher extent of photo-excited electrons for non-radiative relaxation. The $Cu_3(HHTP)_2$ crystalline sheet without Cu metal substrate showed a comparable photothermal conversion performance as $Cu(OH)_2$@Cu. Notably, $Cu_3(HHTP)_2$@Cu exhibited considerably higher surface temperature than $Cu_3(HHTP)_2$ crystal sheet without metal support. This is likely due to the enhanced thermal conductivity provided by the Cu-metal substrate, which optimizes heat dissipation and photothermal conversion performance. Overall, the pronounced photothermal conversion for $Cu_3(HHTP)_2$@Cu is the result of the combined effects of high thermal conductivity of Cu substrate and the photothermal conversion capability of HHTP, where the π-conjugated HHTP ligand played a critical role. Not only HHTP enhances light absorption, but also its extended conjugation system facilitates the non-radiative relaxation processes, leading to enhanced photothermal conversion.

3.5 Cyclic adsorption–desorption performance of $Cu_3(HHTP)_2$@Cu

Leveraging the photothermal effect, the adsorbed NH_3 gas was desorbed from $Cu_3(HHTP)_2$@Cu in a minimally invasive method. The optimal light irradiation time for desorption treatment was determined by measuring the amount of desorbed NH_3 per unit weight of the $Cu_3(HHTP)_2$@Cu with varying irradiation time (Fig. S5†). After 2 h of irradiation, the NH_3 desorption amount reached approximately 4.8 μmol g^{-1}, and longer irradiation time did not produce any significant addition to the desorption amount. Therefore, 2 h was established as the optimal irradiation time. In conventional porous gas adsorbents, the regeneration process typically involves NH_3 desorption under vacuum conditions at elevated temperatures ranging from 100 to 200 °C (Table S1†). In contrast, the present study demonstrates that NH_3 can be desorbed under an ambient N_2 atmosphere simply by 2 h of light illumination, without vacuum application. This highlights a significant advantage of the proposed system as a low-energy regeneration strategy. As shown in Table S1,† the adsorbent developed in this work is particularly noteworthy in that it does not rely on hybridization with external photothermal materials such as in powdery nanomaterials. Instead, it adopts a substrate-supported MOF structure, which is easier to integrate into practical use.

The cyclic adsorption–desorption test was carried out with repeated treatments of 20 h of adsorption in 23 ppm ambient NH_3 concentration and the subsequent 2 h desorption under N_2 ambient condition. This adsorption–desorption process was continued for up to 7 cycles. In the cyclic test, the accumulated NH_3, which represents the NH_3 retained on the MOF, was calculated using eqn (3), where Q_{ad} denotes the NH_3 adsorption amount per cycle, Q_{de} represents the desorbed NH_3 per cycle, and n corresponds to the cycle number.

$$\text{Accumulated } NH_3\,(\mu\text{mol g}^{-1}) = \frac{\sum_{i=1}^{n} Q_{ad} - \sum_{i=1}^{n-1} Q_{de}}{\text{Weight of } Cu_3(HHTP)_2@Cu} \quad (3)$$

Fig. 8a shows the results of the cyclic adsorption–desorption test conducted under various adsorption (Ad) and desorption (De) conditions as illustrated in Table 1. Under all treatments, the additional NH_3 adsorption per cycle decreased as the cycles progressed, and the amount of NH_3 desorbed under each condition reached a plateau in the accumulated NH_3 amount. In Fig. S6a and S6b,† it is evident that the adsorption and desorption amounts approach a steady state after the 4th cycle. Fig. 8a demonstrates that, in the first two cycles, all conditions exhibited comparable adsorption performance. However, as the cycles progressed, the adsorption and desorption performance began to diverge depending on the adsorption and desorption treatment conditions. Compared to the control treatment of $Cu_3(HHTP)_2$@Cu-C, higher amount of NH_3 was desorbed for $Cu_3(HHTP)_2$@Cu-T1 and $Cu_3(HHTP)_2$@Cu-T2 (which underwent NH_3 adsorption without electric voltage) attributed to thermal and photothermal desorption mechanism, and exhibiting higher NH_3 adsorption performance in subsequent adsorption cycles than the control treatment of $Cu_3(HHTP)_2$@Cu-C. The adsorption and desorption amounts for each treatment conditions in the 7th cycle were as follows: $Cu_3(HHTP)_2$@Cu-C (Ad 7.9 μmol g^{-1}, De 6.5 μmol g^{-1}), $Cu_3(HHTP)_2$@Cu-T1 (Ad 23 μmol g^{-1}, De 19 μmol g^{-1}), $Cu_3(HHTP)_2$@Cu-T2 (Ad 24 μmol g^{-1}, De 21 μmol g^{-1}), $Cu_3(HHTP)_2$@Cu-T3 (Ad 17 μmol g^{-1}, De 7.2 μmol g^{-1}). Particularly, NH_3 desorption *via* photothermal conversion ($Cu_3(HHTP)_2$@Cu-T2) was over three times higher than that of control stored at room temperature ($Cu_3(HHTP)_2$@Cu-C), resulting in three times higher adsorption capacity for $Cu_3(HHTP)_2$@Cu-T2 than control.

In contrast, $Cu_3(HHTP)_2$@Cu-T3, despite its enhanced adsorption performance with voltage application, exhibited significantly lower desorption efficiency. In the 7th cycle, the accumulated NH_3 amount was highest for $Cu_3(HHTP)_2$@Cu-T3, reaching 146 μmol g^{-1}. This is attributed to the enhanced NH_3 adsorption performance induced by the applied electric voltage during the adsorption processes. To note, the adsorption experiment conducted under 46 ppm ambient NH_3 concentration (Fig. 2b) also demonstrated the same tendency of enhanced adsorption with external voltage application. However, the desorption performance of $Cu_3(HHTP)_2$@Cu-T3 was as low as that of control, $Cu_3(HHTP)_2$@Cu-C. In comparison, the accumulated NH_3 amount for $Cu_3(HHTP)_2$@Cu-T2 and $Cu_3(HHTP)_2$@Cu-T1 were 108 μmol g^{-1} and 107 μmol g^{-1}, respectively (Fig. 8a), showing similar adsorption–desorption

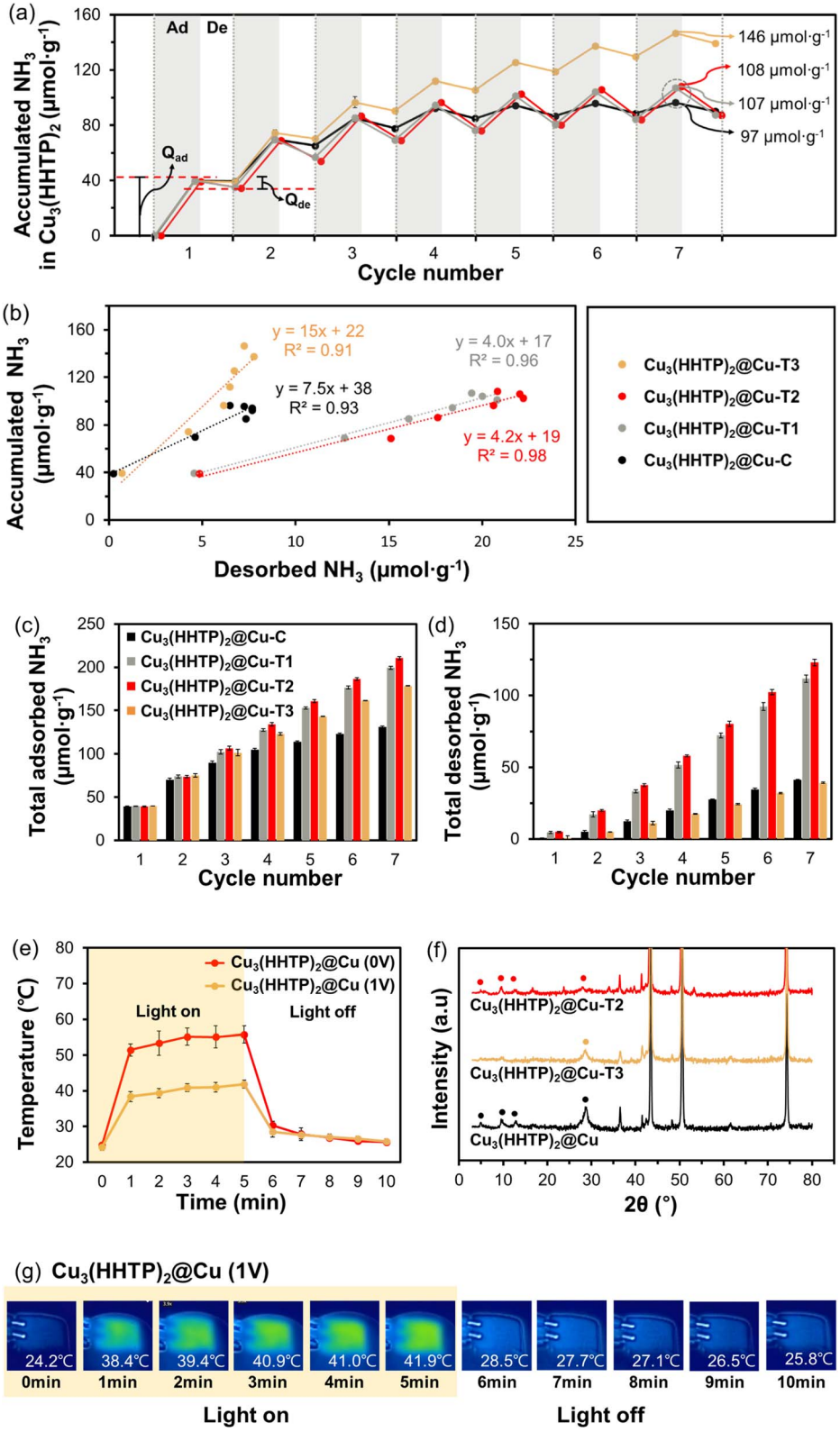

Fig. 8 (a) Cyclic process of NH_3 adsorption–desorption, (b) accumulated NH_3 retained under different treatment conditions, (c) total NH_3 adsorption per cycle (without desorption), (d) total NH_3 desorbed per cycle, (e) photothermal effect with and without 1 V, (f) X-ray diffraction (XRD) patterns of $Cu_3(HHTP)_2$@Cu. (g) Infrared images after 1 V application.

behavior. Among all conditions, the control sample of $Cu_3(HHTP)_2$@Cu-C exhibited the lowest NH_3 accumulation of 97 μmol g^{-1}.

The relationship between the accumulated NH_3 and desorbed NH_3 in each cycle is illustrated in Fig. 8b. The highest accumulation of NH_3 was observed in $Cu_3(HHTP)_2$@Cu-T3, which exhibited superior adsorption but poor desorption performance, producing a steeper slope. Conversely, $Cu_3(HHTP)_2$@Cu-T2 and $Cu_3(HHTP)_2$@Cu-T1 displayed similar adsorption–desorption behavior, as reflected in their nearly identical slope. These results confirm that NH_3 desorption *via* photothermal conversion is primarily driven by the heat converted from the sunlight.

To establish a strategy for repeated use of $Cu_3(HHTP)_2$@Cu as a gas adsorbent, the total adsorbed and desorbed amounts of NH_3 were evaluated from the cyclic tests, using eqn (4) and (5). In the total adsorption calculation, the adsorption in each cycle was all added up without subtracting the desorption amount. As shown in Fig. 8c, during 7 cycles, $Cu_3(HHTP)_2$@Cu-T2 showed the highest total NH_3 adsorption (210 μmol g^{-1}), and the control showed the lowest total NH_3 adsorption (131 μmol g^{-1}). The thermally desorbed sample of $Cu_3(HHTP)_2$@Cu-T1 showed a comparable amount in total adsorption (199 μmol g^{-1}) as $Cu_3(HHTP)_2$@Cu-T2. The $Cu_3(HHTP)_2$@Cu-T3 achieved total adsorption of 179 μmol g^{-1} throughout 7 cycles.

$$\text{Total adsorbed } NH_3\left(\mu\text{mol g}^{-1}\right) = \frac{\sum_{i=1}^{n} Q_{ad}}{\text{Weight of } Cu_3(HHTP)_2@Cu} \quad (4)$$

$$\text{Total desorbed } NH_3\left(\mu\text{mol g}^{-1}\right) = \frac{\sum_{i=1}^{n} Q_{de}}{\text{Weight of } Cu_3(HHTP)_2@Cu} \quad (5)$$

Despite $Cu_3(HHTP)_2$@Cu-T3 retaining the highest accumulated NH_3 within the MOF after 7 cycles (146 μmol g^{-1}), $Cu_3(HHTP)_2$@Cu-T2 demonstrated the highest total NH_3 adsorption, when desorbed amount is ignored. This discrepancy suggests that while electric voltage application enhances overall NH_3 adsorption in $Cu_3(HHTP)_2$@Cu-T3, it simultaneously deteriorates the photothermal-induced desorption efficiency, limiting the available adsorption sites and reducing the additional adsorption in the next cycle. Consequently, the total adsorption of NH_3 was lower for $Cu_3(HHTP)_2$@Cu-T3 than $Cu_3(HHTP)_2$@Cu-T2. Fig. 8d presents that the desorption performance of $Cu_3(HHTP)_2$@Cu-T3 decreased as low as that of control, $Cu_3(HHTP)_2$@Cu-C. In contrast, $Cu_3(HHTP)_2$@Cu-T2 showed the highest amount in total desorption ~123 μmol g^{-1}, three times higher than that of $Cu_3(HHTP)_2$@Cu-T3 (39 μmol g^{-1}).

To explain the deteriorated desorption performance of $Cu_3(HHTP)_2$@Cu after electric voltage application, the photothermal conversion efficiency of $Cu_3(HHTP)_2$@Cu was examined after 1 V was applied to the sample (Fig. 8e). Unlike the original sample that demonstrated efficient photothermal conversion (temperature increase up to ~55 °C), $Cu_3(HHTP)_2$@Cu after 1 V application deteriorated photothermal effect, exhibiting only about 75% of temperature increase (up to ~42 °C). It is noted that $Cu_3(HHTP)_2$ is grown on the $Cu(OH)_2$@Cu surface, and the photothermal performance at the level of $Cu(OH)_2$@Cu indicates the complete loss of photothermal effect induced by the $Cu_3(HHTP)_2$. Due to this decreased photoconversion capability, the desorption performance of $Cu_3(HHTP)_2$@Cu was significantly reduced to the level of control treatment.

The XRD analysis was conducted on $Cu_3(HHTP)_2$@Cu to examine whether any structural deformation is observed after voltage application, which might be the reason for the deteriorated photothermal conversion (Fig. 8f). The X-ray diffraction patterns of $Cu_3(HHTP)_2$@Cu-T2 revealed that, while the peak intensities corresponding to 4.86 [100], 9.76 [200], 12.68 [210], and 28.24 [002] decreased slightly due to the corrosive nature of NH_3, the overall crystalline structure remained intact. However, $Cu_3(HHTP)_2$@Cu-T3 exhibited significant structural deformation, with all diffraction peaks except 28.24 [002] disappearing. This result implicates that the application of 1 V induced structural modifications in $Cu_3(HHTP)_2$. Due to the structural modification, the interactions in π–π conjugation of the HHTP ligands may be weakened, consequently impairing photothermal conversion efficiency and desorption performance. Notably, despite the deformed crystalline structure, $Cu_3(HHTP)_2$@Cu-T3 (after voltage application) demonstrated higher BET surface area, allowing the high capacity for NH_3 adsorption, than $Cu_3(HHTP)_2$@Cu-T2 (without voltage application). While electric applications increased the BET and enlarged the adsorption capacity, it deteriorated the photothermal conversion efficiency. Thus, for the long-term use of $Cu_3(HHTP)_2$@Cu adsorbents, minimized structural modification of MOF would be beneficial to maintain efficient photothermal conversion and gas desorption performance. The results demonstrate that $Cu_3(HHTP)_2$@Cu can be photothermally recyclable, which is a sustainable and energy-efficient strategy for NH_3 release, ensuring the effective regeneration of adsorption sites over multiple cycles.

4. Conclusions

This study demonstrates the potential of $Cu_3(HHTP)_2$@Cu as a recyclable NH_3 gas adsorbent by leveraging its photothermal conversion for efficient and minimally invasive gas desorption. The *in situ* synthesis of $Cu_3(HHTP)_2$ employs a Cu mesh substrate as both a structural support and a Cu metal precursor. Given that $Cu_3(HHTP)_2$ had porous characteristics and unsaturated Cu sites, $Cu_3(HHTP)_2$@Cu exhibited adsorption performance for NH_3. When an electric voltage of 1 V was applied, NH_3 adsorption performance was further enhanced by increasing the proportion of coordinatively unsaturated Cu sites and strengthening the interaction between NH_3 and $Cu_3(HHTP)_2$@Cu. Additionally, $Cu_3(HHTP)_2$@Cu, supported by the metal mesh, demonstrated higher photothermal conversion performance than $Cu_3(HHTP)_2$ crystalline, attributed to the

high thermal conductivity of the Cu substrate. This photothermal conversion facilitated efficient NH_3 desorption under light exposure, eliminating the need for heating conditions or energy input. Cyclic adsorption–desorption tests showed that photothermal desorption significantly improved the long-term usability of $Cu_3(HHTP)_2$@Cu for NH_3 adsorption. While applied voltage improved an initial NH_3 uptake of $Cu_3(HHTP)_2$@Cu, it also induced irreversible structural deformation that hindered efficient desorption. The DFT simulation reveals that NH_3 binds more strongly to $Cu_3(HHTP)_2$ under electron-rich conditions, implying a charge-mediated adsorption mechanism. This study presents a promising approach for the repeated use of $Cu_3(HHTP)_2$-based adsorbents with efficient gas desorption strategies. By enabling efficient regeneration of adsorption sites *via* photothermal conversion, $Cu_3(HHTP)_2$@Cu demonstrates strong potential for sustainable and energy-efficient NH_3 removal systems, offering an informative discussion for further advancing photothermal-assisted gas desorption technologies.

Data availability

The data that support the findings of this study are available in the ESI document.† Also, they will be available upon request to the corresponding author.

Conflicts of interest

The authors declare there are no conflicts of interest.

Acknowledgements

This work was supported by the National Research Foundation of Korea (NRF) grant funded by the Korea government (MSIT) (No. RS-2024-00405333; RS-2025-00523094).

References

1 B. Han, C. Butterly, W. Zhang, J.-z. He and D. Chen, *J. Cleaner Prod.*, 2021, **283**, 124611.
2 Y. Sun, X. Zhang, M. Zhang, M. Ge, J. Wang, Y. Tang, Y. Zhang, J. Mi, W. Cai, Y. Lai and Y. Feng, *Chem. Eng. J.*, 2022, **446**, 137099.
3 W. Zhang, G. Li, H. Yin, K. Zhao, H. Zhao and T. An, *Environ. Sci.: Nano*, 2022, **9**, 81.
4 X. Wang, R. Su, Y. Zhao, W. Guo, S. Gao, K. Li, G. Liang, Z. Luan, L. Li, H. Xi and R. Zou, *ACS Appl. Mater. Interfaces*, 2021, **13**, 58848.
5 T. Z. San, J. H. Park, M. Z. Win, L. S. D. Ugli, W. Oo and K. B. Yi, *Sep. Purif. Technol.*, 2025, **353**, 128560.
6 T. Yan, T. X. Li, R. Z. Wang and R. Jia, *Appl. Therm. Eng.*, 2015, **77**, 20.
7 T. Jia, Y. Gu and F. Li, *J. Environ. Chem. Eng.*, 2022, **10**, 108300.
8 L. Jiao, J. Y. R. Seow, W. S. Skinner, Z. U. Wang and H.-L. Jiang, *Mater. Today*, 2019, **27**, 43.
9 T. He, X.-J. Kong and J.-R. Li, *Acc. Chem. Res.*, 2021, **54**, 3083.
10 C. Gao, J. Wang, H. Xu and Y. Xiong, *Chem. Soc. Rev.*, 2017, **46**, 2799.
11 M. Woellner, S. Hausdorf, N. Klein, P. Mueller, M. W. Smith and S. Kaskel, *Adv. Mater.*, 2018, **30**, 1704679.
12 X. Wang, Z. Liu, G. Li, G. Jiang, Y. Zhao, L. Li, K. Li, G. Liang, S. Gao, H. Xi, S. Li and R. Zou, *Chem. Eng. J.*, 2022, **440**, 135764.
13 J. Li, R. J. Kuppler and H. Zhou, *Chem. Soc. Rev.*, 2009, **38**(5), 1477.
14 T. Yoskamtorn, P. Zhao, X.-P. Wu, K. Purchase, F. Orlandi, P. Manuel, J. Taylor, Y. Li, S. Day, L. Ye, C. C. Tang, Y. Zhao and S. C. E. Tsang, *J. Am. Chem. Soc.*, 2021, **143**, 3205.
15 Y. Yang, T. Zhang, T. Wang, T. Zhou, Y. Belmabkhout, Q. Gu and J. Shang, *Small Sci.*, 2025, 2400391.
16 S. Li, S. Subhan, L. Zhou, J. Li, Z. Zhao and Z. Zhao, *Chem. Eng. J.*, 2023, **465**, 142791.
17 X. Wang, X. Zhang, A. He, J. Guo and Z. Liu, *Inorg. Chem.*, 2024, **63**, 6948.
18 E. Borfecchia, S. Maurelli, D. Gianolio, E. Groppo, M. Chiesa, F. Bonino and C. Lamberti, *J. Phys. Chem. C*, 2012, **116**, 19839.
19 B. E. R. Snyder, A. B. Turkiewicz, H. Furukawa, M. V. Paley, E. O. Velasquez, M. N. Dods and J. R. Long, *Nature*, 2023, **613**, 287.
20 P. Zhou, Z. Li, Z. Wang, H. Wang, Y. Zhao and J. Wang, *Sep. Purif. Technol.*, 2024, **336**, 126348.
21 Y. C. Kang and R. D. Ramsier, *Vacuum*, 2001, **64**, 113.
22 Y. Li, X. Kong, D. Zhu, T. Guo, X. Wu, W. Yu and L. Wang, *Sep. Purif. Technol.*, 2025, **360**, 131193.
23 H. Liu, N. Li, M. Feng, G. Li, W. Zhang and T. An, *Environ. Sci.: Nano*, 2022, **9**, 1858.
24 J. Zhou, H. Liu and H. Wang, *Chin. Chem. Lett.*, 2023, **34**, 107420.
25 S. Ullah, N. Ullah, S. S. Shah, D. Guziejewski, F. Khan, I. Khan, A. Ahmad, M. Saeed, S. Khan and F. Mabood, *Renewable Sustainable Energy Rev.*, 2024, **201**, 114615.
26 H. Mai, D. Chen, Y. Tachibana, H. Suzuki, R. Abe and R. A. Caruso, *Chem. Soc. Rev.*, 2021, **50**, 13692.
27 S. R. Shewchuk, A. Mukherjee and A. K. Dalai, *Chem. Eng. Sci.*, 2021, **243**, 116735.
28 Y. Xiao, H. Guo, M. Li, J. He, X. Xu, S. Liu, L. Wang and T. D. James, *Coord. Chem. Rev.*, 2025, **527**, 216378.
29 W. Lan, X. Gou, Y. Wu, N. Liu, L. Lu, P. Cheng and W. Shi, *Angew. Chem., Int. Ed.*, 2024, **63**, e202401766.
30 K. Gayathri, K. Vinothkumar, Y. N. Teja, B. M. Al-Shehri, M. Selvaraj, M. Sakar and R. G. Balakrishna, *Colloids Surf., A*, 2022, **653**, 129992.
31 T. N. Nguyen, F. M. Ebrahim and K. C. Stylianou, *Coord. Chem. Rev.*, 2018, **377**, 259.
32 S. Zahra Haeri, M. Khiadani, B. Ramezanzadeh, H. Kariman and M. Zargar, *Appl. Therm. Eng.*, 2025, **258**, 124607.
33 T. Liu, X. Zhang, H. Wang, M. Chen, Y. Yuan, R. Zhang, Z. Xie, Y. Liu, H. Zhang and N. Wang, *Chem. Eng. J.*, 2021, **412**, 128700.
34 A. M. Pornea and H. Kim, *Sol. Energy Mater. Sol. Cells*, 2022, **244**, 111817.

35 S. Zhu, C. Huang, X. Li, X. Chen, H. Ye, Z. Xue, W. Hu and T. Wang, *Aggregate*, 2024, **5**, e529.
36 M. Gao, L. Zhu, C. K. Peh and G. W. Ho, *Energy Environ. Sci.*, 2019, **12**, 841.
37 C. Li, L. Zhang, J. Chen, X. Li, J. Sun, J. Zhu, X. Wang and Y. Fu, *Nanoscale*, 2021, **13**, 485.
38 M. d. L. Gonzalez-Juarez, M. A. Isaacs, D. Bradshaw and I. Nandhakumar, *ACS Appl. Mater. Interfaces*, 2023, **15**, 5478.
39 J. Ren, W. Zhang, Z. Xuan, L. Li and W. Yuan, *J. Energy Storage*, 2024, **79**, 110180.
40 I. S. Khan, L. Garzon-Tovar, D. Mateo and J. Gascon, *Eur. J. Inorg. Chem.*, 2022, **2022**, e202200316.
41 L. Lüder, A. Gubicza, M. Stiefel, J. Overbeck, D. Beretta, A. Sadeghpour, A. Neels, P. N. Nirmalraj, R. M. Rossi, C. Toncelli and M. Calame, *Adv. Electron. Mater.*, 2022, **8**, 2100871.
42 X. Yin, Y. Li, W. Cai, C. Fan, W. Liu, N. Wang, G. Qin, Z. Xie, X. Chen and Y. Han, *Appl. Surf. Sci.*, 2023, **624**, 157124.
43 W. He, L. Zhou, M. Wang, Y. Cao, X. Chen and X. Hou, *Sci. Bull.*, 2021, **66**, 1472.
44 A. J. Rieth, Y. Tulchinsky and M. Dincă, *J. Am. Chem. Soc.*, 2016, **138**, 9401.
45 J.-D. Xiao and H.-L. Jiang, *Acc. Chem. Res.*, 2019, **52**, 356.
46 J. Qu, S. Li, B. Zhong, Z. Deng, Y. Shu, X. yang, Y. Cai, J. Hu and C. M. Li, *Nanoscale*, 2023, **15**, 2455.
47 X. Cui, Q. Ruan, X. Zhuo, X. Xia, J. Hu, R. Fu, Y. Li, J. Wang and H. Xu, *Chem. Rev.*, 2023, **123**, 6891.
48 J. J. P. Stewart, *J. Mol. Model.*, 2007, **13**, 1173.
49 H. Lim, H. Kwon, H. Kang, J. E. Jang and H.-J. Kwon, *Nat. Commun.*, 2023, **14**, 3114.
50 V. Sydorchuk, O. I. Poddubnaya, M. M. Tsyba, O. Zakutevskyy, O. Khyzhun, S. Khalameida and A. M. Puziy, *Appl. Surf. Sci.*, 2021, **535**, 147667.